Applications in Energy and Combustion Science 25 (2026) 100435

Contents lists available at ScienceDirect

Applications in Energy and Combustion Science

journal homepage: www.elsevier.com/locate/jaecs

Investigation of ethanol blending on soot particle evolution in counterflow diffusion flames of a gasoline surrogate ☆

Fenja Ahrendt [a,1], Robert Schmitz [a,1], Fabian P. Hagen [b], Petros Vlavakis [b], Dimosthenis Trimis [b], Federica Ferraro [a,*]

[a] Institute of Jet Propulsion and Turbomachinery (IFAS), Technische Universität Braunschweig, Braunschweig, Germany
[b] Engler-Bunte-Institute, Karlsruhe Institute of Technology (KIT), Karlsruhe, Germany

ARTICLE INFO

Keywords:
Ethanol
Gasoline surrogate
Soot formation
Soot modeling
Split-based Extended Quadrature Method of Moments (S-EQMOM)

ABSTRACT

Across all transport sectors, there is an increasing recognition of the importance of reducing not only CO_2 emissions but also other climate-impacting pollutants, such as soot particulate matter. Ethanol, a widely utilized biofuel, has the potential to significantly reduce CO_2 emissions. However, its influence on soot formation when blended with complex hydrocarbon fuels remains unclear. Previous studies showed that blending ethanol above 40 vol% reduces both the total soot volume fraction and particle diameter, while at lower blending ratios, 20 vol% ethanol or less, discrepant trends can be found in the literature. In some studies, a synergistic effect has been observed, where ethanol blending with various hydrocarbon fuels promotes soot formation. To address these uncertainties, this study investigates the effects of varying ethanol blending ratios with a gasoline surrogate (90 vol% iso-octane and 10 vol% toluene) on soot formation characteristics in a laminar counterflow diffusion flame for ethanol ratios up to 60 vol%. Experimental and numerical investigations are conducted to understand the effects of ethanol blending on gas-phase products, soot volume fraction and particle size distribution. Gas-Chromatography and two-color Time-Resolved Laser Induced Incandescence (TR-LII) were employed to measure gas species, soot volume fraction and primary particle size distribution, respectively. Numerical simulations are carried out using a detailed soot model based on the Split-based Extended Quadrature Method of Moments (S-EQMOM). Both experimental and numerical results consistently show a non-linear impact of ethanol blending on soot precursors and a non-monotonic effect on particle quantities. Small amounts of ethanol, up to 10 vol%, have little effect on soot formation. However, higher levels of ethanol significantly reduce soot formation and the diameter of large particles. Analysis of individual soot processes reveals that, when ethanol is added, PAH-related soot processes, such as inception and PAH-deposition, are the limiting steps, while the HACA and soot oxidation mechanisms are less affected.

1. Introduction

Anthropogenic emissions, including CO_2, NO_x, and soot, which are primarily produced by the combustion of fossil hydrocarbons, are a major driver of climate change [1]. Despite global efforts to reduce emissions by scaling up renewable energy sources and electrification, fossil fuels still supply about 80 % of global energy consumption [2]. One promising pathway to reduce carbon emissions is to use bio-derived oxygenated hydrocarbons or biofuels, which can enable a carbon-neutral energy balance. Accordingly, biofuels, such as bio-ethanol and bio-butanol, have been extensively investigated as an alternative to fossil fuels over the past decades [3,4], showing the potential to reduce not only CO_2 but also soot emissions [5,6]. Soot emissions are considered a significant contributor to climate forcing, ranking second in impact [7]. Soot particles are not only detrimental to the environment but also harmful to human health. Specifically, ultrafine particles can be inhaled, absorbed by lung cells, and enter the circulatory system, reaching organs such as the liver and heart [8].

One advantage of biofuels is that they can be used in existing engines, or with minimal modifications, and could even enhance the engine efficiency [9]. Ethanol is currently the most widely used biofuel [9], commonly blended at low concentrations with gasoline for spark-ignition engines. Several studies have explored its combustion

☆ This article is part of a Special issue entitled: 'Women in Combustion2' published in Applications in Energy and Combustion Science.

* Corresponding author.
E-mail address: federica.ferraro@tu-braunschweig.de (F. Ferraro).
[1] Joint First Authors.

https://doi.org/10.1016/j.jaecs.2025.100435
Received 28 June 2025; Received in revised form 15 November 2025; Accepted 27 November 2025
Available online 27 November 2025

and emission characteristics in various canonical flame configurations [10–13] as well as in engine tests [14]. Koegl et al. [14] investigated the formation and oxidation of soot in ethanol and butanol fuel blends in a direct-injection spark-ignition engine at ethanol and butanol ratios of 20 %. An increase in the formation of soot for both oxygenated fuels was observed.

Recently, Do et al. [15] studied turbulent diffusion flames of different gasoline mixtures with varying ethanol ratios between 0 to 100 %. Soot formation decreased quasi-linearly with increasing ethanol ratios up to 40 %. No linear relation was observed beyond this point and no more soot particles were detectable at 85 %.

To conduct fundamental investigations on soot formation from various fuels and their blends, lab-scale laminar flames are often employed for their very well-defined boundary conditions and setup simplicity, which enable also numerical modeling and detailed simulations. Salamanca et al. [10] experimentally investigated laminar premixed ethylene flames blended with ethanol ratios up to 30 %. They found that as the amount of ethanol increases, the formation of soot particles decreases. A correlation was also identified between the reduction of soot and the equivalence ratio: the soot reduction effect increased for lower equivalence ratios. Additional analysis of particle size distributions in blended and unblended flames suggested that ethanol blending might either reduce coagulation efficiency or slow nanoparticle formation and growth mechanisms. In a counterflow diffusion configuration with a soot formation type of flame, similar effects as in the premixed flame are produced on the oxidizer side of the stagnation plane when ethanol is used as a substituent in the fuel stream, as reported in Salamanca et al. [11]. On the fuel side, adding low amounts of ethanol up to 20 vol% increased nanoparticle and soot formation, while larger amounts led to a reduced formation of larger particles [11]. This enhancement at low ethanol blending was attributed to increased fuel reactivity in the pyrolytic zone, which ultimately promotes polycyclic aromatic hydrocarbon (PAH) formation and growth, while higher amounts of ethanol result in enhanced fuel oxidation [11]. Similarly, Frenzel et al. [12] experimentally investigated ethanol blends up to neat ethanol in laminar premixed iso-octane/air flames. A reduction in the volume fraction and particle diameter of soot could be observed, while the number of particles remained in the same range.

McNesby et al. [16] examined the soot formation mechanism in ethylene counterflow flames to which ethanol was added up to 8 % on both the oxidizer and the fuel sides. Adding ethanol to the oxidizer side resulted in premixed combustion, creating a secondary flame zone prior to the main flame zone. Due to the convection of OH and other hot gas products into the primary flame zone, the peak temperature increased and the OH concentration profile expanded. As a result, the soot precursor and soot oxidation increased, which decreased the overall soot concentration. In contrast, the soot concentration increased when adding ethanol to the fuel side. The lack of oxygen in the fuel stream caused the ethanol to decompose via pyrolysis, leading to the production of methyl radical (CH_3) in the initial steps and an increased production of benzene (A1).

The effects of ethanol addition on PAHs and soot in counterflow diffusion flames of ethylene was further investigated experimentally and numerically by Yan et al. [9]. A synergistic effect of ethanol addition on soot concentration was observed for lower blending ratios. The reaction pathway analysis indicated that ethanol blends enhance the formation of CH_3 radicals and C_3H_3. This reaction pathway could promote the formation of benzene and larger aromatics leading to increased soot formation for low ethanol blending ratios.

The influence of the strain rate on soot and nanoparticle formation was investigated in laminar counterflow flames of ethylene blended with ethanol and oxymethylene ethers (OMEs) by Esposito and Sirignano [17]. The study revealed that both nanoparticles and soot were formed in the pyrolytic and oxidative zone, while smaller particle sizes were observed in the pyrolytic zone. The amount of particles decreased with increasing strain rates. Additionally, a slight increase of nanoparticles was detected in the pyrolytic zones of ethanol-blended flames.

To investigate the effects of oxygenated fuels at low blending ratios, McEnally and Pfefferle [18] experimentally examined the addition of 10 % dimethyl ether and ethanol to an ethylene laminar coflowing flame under atmospheric condition and compared with pure oxygenated fuel flames. The results showed that blending oxygenated fuels enhances soot formation compared to neat ethylene flames, even though pure oxygenated fuel flames show negligible soot formation. More recently, Yang et al. [19] and Lyu et al. [13] investigated soot formation at elevated pressure in laminar coflowing flames of ethylene and n-heptane, respectively, with increasing ethanol concentrations. Similar to [9], both studies reported enhanced soot formation at 10 % ethanol blending, while a significant reduction was observed at 20 % and higher ethanol blending, also at elevated pressure.

In summary, although ethanol generally decreases soot formation, numerous studies have reported increased soot emissions at low blending ratios (around 10–20 %) [13,14,17–19], depending on multiple factors such as fuel dilution, flame temperature, pressure and configuration. Most existing studies have focused on ethanol blended with ethylene, and only a few studies [11,17] have analyzed both soot volume fraction and particle size distribution.

Therefore, this work provides a thorough examination of how adding ethanol to a gasoline surrogate affects soot formation in a counterflow diffusion flame. Combined experimental and numerical analyses focus on gas phase, soot volume fraction, and particle size distribution to provide a comprehensive understanding of the sooting behavior of complex blended hydrocarbon fuels. Although this well-controlled canonical flame configuration does not reproduce all physical phenomena present in a real engine, it allows to focus on fuel chemical effects separated from other processes. Specifically, the objectives are: (i) to present a comprehensive dataset of ethanol blends in gasoline surrogate over a wide range of blending ratios, between 0 and 60 %, with a particular emphasis on the low blending ratios, and (ii) to understand the conflicting trends in soot formation described above by exploring the effects of ethanol blending on soot precursors, nanoparticles and larger particles.

Non-premixed laminar counterflow diffusion flames with constant conditions of strain, carbon stream, and flame positions are investigated. A gasoline surrogate consisting of toluene and iso-octane is employed. Gas-phase major species and soot precursors are measured using Gas-Chromatography, while soot characteristics are evaluated using two-color Time-resolved Laser Induced Incandescence (2C-TiRe-LII) [20,21]. The numerical simulations are performed using an advanced soot model based on the Split-based Extended Quadrature Method of Moments (S-EQMOM) [22], which allows for the reconstruction of the particle size distribution.

The structure of this work is as follows. First, the investigated flame conditions are described. Then, the experimental approach is presented, followed by the numerical modeling approach. The results section includes experimental and numerical comparisons of the flame structure, gas phase species, soot volume fractions, and particle size distributions. Finally, detailed analyses of the contributions of individual soot processes are presented.

2. Overview of investigated flames

In this study, laminar counterflow diffusion flames burning a gasoline surrogate mixed with different amounts of ethanol (C_2H_5OH) are investigated. The stoichiometric mixture fraction, temperatures of fuel and oxidizer streams, strain rate, and composition of the oxidizer stream are kept constant in order to isolate the influence of the ethanol content in the fuel on the kinetics and soot formation processes. The gasoline surrogate consists of iso-octane (iC_8H_{18}) and toluene (C_7H_8) with a fixed volume ratio of 9:1. Toluene is chosen as a representative aromatic compound of gasoline fuel to guarantee sooting

Table 1
Ethanol content in the fuel mixture (in vol%), fuel composition of investigated flames in mole fraction, atomic ratios of the fuel stream and maximum temperatures.

Flame	Surrogate in vol%	Fuel stream composition in mole fractions				Atomic ratios		Maximum temperature in K	
	C_2H_5OH	C_2H_5OH	C_7H_8	iC_8H_{18}	N_2	C/H	C/O	Numerical	Experimental
EthOHX00	0	0.000	0.031	0.177	0.792	0.476	∞	1822	1837
EthOHX05	5	0.028	0.030	0.170	0.772	0.469	58.1	1828	1852
EthOHX10	10	0.056	0.029	0.162	0.753	0.462	28.8	1832	1839
EthOHX20	20	0.119	0.027	0.150	0.704	0.448	13.7	1845	1859
EthOHX40	40	0.248	0.021	0.118	0.613	0.420	6.40	1864	1883
EthOHX60	60	0.402	0.015	0.085	0.498	0.391	3.95	1887	1885

conditions. Iso-octane mimics the principal combustion properties of gasoline fuel. The gasoline surrogate is blended with increasing amount of ethanol, from 0 vol% to 60 vol%. In addition, the fuel mixtures are diluted by N_2 to maintain a constant stoichiometric mixture fraction of $Z_{st} = 0.1$ across all flames. This ensures that the position of the flame and the temperature peak remain similar in all investigated flames. The mixture compositions were chosen to isolate the effects of the fuel composition on polycyclic aromatic hydrocarbons (PAHs) and subsequent soot formation processes from the effects of temperature. Table 1 summarizes the fuel stream compositions in molar fractions for all investigated flames, including the respective C_2H_5OH content, the C/H and C/O atomic ratios, the maximum flame temperature and the naming convention adopted. The oxidizer stream consists of air, while a simplified composition of $X_{N_2} = 0.79$ and $X_{O_2} = 0.21$ is specified in the numerical simulations. The temperatures of the fuel and oxidizer stream at their corresponding inlets are $T_{fuel} = 393\,\mathrm{K}$ and $T_{ox} = 298\,\mathrm{K}$, respectively.

To ensure that the gas-phase stagnation plane is located approximately in the middle between the fuel and oxidizer ducts, a momentum balance of the inlet streams is established for all flames. A constant strain rate of $K = 60\,\mathrm{s}^{-1}$, calculated on the basis of the velocity u_{ox} of the oxidizer stream, is chosen for all flames. Hereby, the global strain rate definition provided by Seshadri and Williams [23] is applied and further simplified by the momentum balance of both inlet streams, leading to the correlation

$$K = 4u_{ox}/L. \tag{1}$$

3. Experimental approach

A counterflow burner developed by Niemann, Seshadri and Williams [24] was used to stabilize laminar counterflow diffusion flames at atmospheric pressure. It consists of two water-cooled opposing ducts with an inner diameter of 25 mm and a fixed separation distance of 12.5 mm. The fuel is introduced through the lower duct, while the oxidizer, ambient air in this study, is supplied from the top. Both ducts are shielded by nitrogen sheath flows. Fine wire meshes at the duct exits ensure near plug-flow conditions. The liquid fuel is evaporated using a syringe pump and a direct vaporizer system [25,26]. Depending on the target fuel composition, a defined nitrogen flow is added downstream of the vaporizer. All fuel lines are heated to 400 K to prevent condensation.

The axial temperature profiles were measured using an S-type thermocouple probe as described in [27]. A spring mechanism prevents deformation of the thin thermowires with a diameter of 100 µm, which are fixed under tension and aligned parallel to the reaction zone. To eliminate catalytic effects, the wires were coated with zirconium oxide. The coated thermocouple bead has a diameter of 400 µm. The measured temperatures were corrected for radiation losses according to Shaddix [28]. Considering the standard deviation of the measurement and the uncertainties imposed by the radiation correction, the uncertainty of the reported temperatures is 80 K [21,25–27].

A gas chromatograph (GC) with multiple detectors was used to determine the spatially resolved gas-phase composition. Sampling was carried out using a ceramic microprobe with an inner diameter of 300 µm and an outer diameter of 500 µm, directly connected to the GC and based on a design originally proposed by Carbone and Gomez [29]. The microprobe was inserted horizontally into the counterflow flames. Vertical movement along the flame axis was enabled by the traversable counterflow burner. A CCD camera monitored the probe position. While no visible disturbance of the flame was observed, the method introduces a spatial uncertainty of ± 500 µm. The transfer line was heated to 423 K to prevent condensation. The GC, described in detail elsewhere [25,30], used three dedicated columns with thermal conductivity detectors to quantify CO, CO_2, O_2, H_2, and H_2O. A fourth column was used to separate lighter and heavier hydrocarbons. These fractions were analyzed using two additional GC columns, each connected to flame ionization detectors and mass spectrometry. The GC system including all detectors was calibrated using certified gas and liquid standards. The uncertainties are 3 % to 10 % for major species, 5 % to 30 % for hydrocarbons including aromatics, and 20 % for H_2O.

The soot volume fraction and the primary particle size distribution (PSD) were determined by two-color time-resolved laser-induced incandescence (2C-TiRe-LII). The temperature rise of a particle ensemble upon laser pulse absorption is governed by the energy balance:

$$\frac{N\,\pi\,\rho_p}{6}\int_0^\infty\left[\int_{T_p^0}^{T_p^*} d_p^3\,c_s\,\mathrm{PSD}\,dT\right]dd_p = \frac{N\,\pi^2\,E(m,\lambda_{exc})\,f_{exc}}{\lambda_{exc}}\int_0^\infty d_p^3\,\mathrm{PSD}\,dd_p. \tag{2}$$

Here, T_p denotes the particle temperature, with T_p^0 and T_p^* referring to the states before and after laser pulse absorption, respectively. The parameters ρ_p, d_p, N, and c_s represent the particle density, size, number, and volumetric heat capacity. Following [31,32], the PSD is best approximated by a log-normal distribution; in line with [20,21], we assume a geometric standard deviation of 1.4. Although developing geometric standard deviations have been reported in [20], the overall trends of the count median diameter remain robust against the chosen assumption, which justifies the use of a constant value in this study. In Eq. (2), λ_{exc} denotes the excitation wavelength and f_{exc} the laser fluence integrated over the pulse. The absorption function $E(m,\lambda_{exc})$ accounts for the complex refractive index m at the excitation wavelength. Assuming temperature-independent volumetric heat capacity, $E(m,\lambda_{exc})$ can be inferred from pre- and post-pulse temperature measurements, as reported in [33,34]. The evolution of soot maturity during particle formation can thereby be monitored directly through $E(m,\lambda_{exc})$ [35,36]. The temperature of the laser-heated soot particle ensemble is derived from Planck's radiation law. Under homogeneous and optically thin conditions within the laser probe volume, the thermal emission signal $S(\lambda_d,T_p)$ at a discrete detection wavelength λ_d follows Planck's law integrated over all solid angles [31]:

$$S(\lambda_d,T_p) = N\int_0^\infty \frac{8\pi^3 h c_\lambda^2\,E(m,\lambda_d)\,\Sigma_d\,d_p^3\,\mathrm{PSD}}{\lambda_d^6} \times\left[\exp\left(\frac{hc_\lambda}{\lambda_d k_B T_P}\right)-1\right]^{-1} dd_p. \tag{3}$$

The spectral sensitivity of the detection system is accounted for by Σ_d. Here, k_B denotes Boltzmann's constant, h Planck's constant, and c_λ the speed of light. Assuming Wien's approximation, i.e., $\exp\left(hc_\lambda/\lambda_d k_B T_p\right)$

$\gg 1$ [37], the particle temperature can be derived from the ratio of signals $S(\lambda_d^i, T_p)$ and $S(\lambda_d^{ii}, T_p)$ measured at two detection wavelengths λ_d^i and λ_d^{ii}, respectively [31,38].

$$T_p = \frac{hc_\lambda}{k_B}\left(\frac{1}{\lambda_d^{ii}} - \frac{1}{\lambda_d^i}\right) \times \left[\ln\left(\frac{S(\lambda_d^i, T_p)\, E(m, \lambda_d^{ii})\,(\lambda_d^i)^6}{S(\lambda_d^{ii}, T_p)\, E(m, \lambda_d^i)\,(\lambda_d^{ii})^6}\right) C_{cal}\right]^{-1} \quad (4)$$

The calibration constant C_{cal}, accounting for the relative spectral sensitivity of the detection system at both wavelengths, is determined using a tungsten lamp [21,33].

Following laser pulse absorption and the associated prompt temperature rise, the gas-borne particle ensemble cools down to the ambient gas temperature. In the low-fluence regime of 2C-TiRe-LII, particle cooling is governed by heat conduction [38]. Since the conductive cooling rate scales with surface area, smaller particles cool faster than larger ones. As a result, the temporal decay of particle temperature – measured by 2C pyrometry, see Eq. (4) – reflects the primary particle size distribution. The decay, which depends non-linearly on the PSD moments, is simulated numerically using an energy balance. Assuming a log-normal PSD, the statistical moments of the actual PSD are retrieved via multidimensional nonlinear fitting of the simulated decays to those measured experimentally [39]. In this work, the energy balance includes source terms based on the Karlsruhe model [21,33].

The experimental quantification of the primary particle size distribution from 2C-TiRe-LII decays is subject to several sources of uncertainty. The fit quality between measured decay curves and the Karlsruhe model contributes about 2 % to 5 %. A major systematic contribution arises from the assumption of the geometric standard deviation by up to 15 %. Additional contributions result from uncertainties in the local gas temperature of about 3 % and detector linearity below 2 %. Furthermore, the choice of optical properties used in the evaluation introduces an additional systematic contribution of roughly 10 %, while variations in particle morphology may further influence heat transfer and optical properties in ways that are difficult to isolate quantitatively. Considering all contributions, the combined standard uncertainty of the count median diameter is estimated at about 15 %. This range is consistent with comparisons to transmission electron microscopy data reported in the literature [40]. To remain conservative, the count median diameter of the primary particle size distribution is therefore reported with an expanded uncertainty of less than 20 % with a coverage factor of two.

In the Rayleigh regime, laser pulse absorption by particles is proportional to their volume within the detection volume. According to Kirchhoff's law, thermal radiation follows the same scaling. Hence, 2C-TiRe-LII also enables the quantification of the soot volume fraction, provided that all particles are heated uniformly regardless of size. This condition is met by operating in the plateau regime [38], not in the low-fluence regime. Under these conditions, the peak signal is approximately proportional to the soot volume fraction. The corresponding calibration constant is determined using reference flames with known soot volume fraction. As mentioned above, flame-specific and spatially resolved values of $E(m, \lambda_{exc})$ were retrieved from low-fluence 2C-TiRe-LII evaluations based on pre- and post-pulse temperature measurements [33,34]. The plateau-calibrated soot volume fractions were subsequently corrected using these values to account for differences between the reference flame and the investigated counterflow diffusion flames. This ensures that variations in optical properties are reflected in the evaluation of soot volume fractions. Although such corrections reduce systematic errors, residual uncertainties remain and are explicitly accounted for. According to [21], the uncertainty in soot volume fraction can reach up to 40 % due to repeatability and sensitivity to $E(m, \lambda_{exc})$. For soot volume fractions above 500 ppb and $E(m, \lambda_{exc}) > 0.3$, the uncertainty decreases to below 20 %.

The calibration constant used to quantify the soot volume fraction was determined by comparing the measured $S^*(\lambda_d^{ii})$ from our laser-optical setup with values obtained in a laminar, premixed ethylene/air reference flame at 2.1, for which the soot volume fraction is known from Hadef et al. [41]. The values of $E(m, \lambda_{exc})$ were taken from [35] and verified against our measurements, showing good agreement.

In this study, a Q-switched Nd:YAG laser, operating at 10 Hz and at $\lambda_{exc} = 1064$ nm, was used. A rotating half-wave plate combined with a polarizing beam splitter ensured a well-defined fluence. Pulse-to-pulse fluence was monitored using a calibrated fast photodiode, while the total laser energy was measured with an energy sensor. The beam passed through a mirror array and aperture and was relay-imaged into the detection volume with 1:1 magnification. 2C-TiRe-LII signal decays were recorded at 120° to the laser axis using a 2C detection system consisting of a lens assembly and two fast photomultipliers equipped with 10 nm FWHM interference filters centered at $\lambda_d^i = 450$ nm and $\lambda_d^{ii} = 650$ nm. Signals were recorded using an oscilloscope, triggered by photodiode used for fluence monitoring. Further details on the setup are given in [20,21,33].

4. Numerical approach

Numerical calculations of the laminar counterflow diffusion flames are performed using the Universal Laminar Flame (ULF) solver [42] on a one-dimensional domain. Finite-rate chemistry is applied for the modeling of the gas-phase species. Soot particle formation is modeled using the S-EQMOM [22]. Both the chemical kinetics and the soot modeling approach are further elaborated in the subsequent sections.

4.1. Gas-phase modeling

The chemical kinetics of the gas-phase species is modeled using a semi-detailed reaction mechanism based on the DLR Concise mechanism [43,44]. It covers the decomposition and oxidation of the fuel species described above and also includes the formation kinetics of the soot precursor species. In addition to this base mechanism, reaction kinetics of the formation pathways of polycyclic aromatic hydrocarbons up to pyrene (A4) were updated in [43,44]. Pyrene is the largest PAH species explicitly considered in the gas-phase mechanism, which accounts for all larger PAHs as a lumped species, similar to previous studies, e.g. [45,46]. This ensures consistency in the combination of kinetics and the inception step in soot modeling, with pyrene linking the gas-phase chemistry to the soot particle modeling. In total, the mechanism contains 214 chemical species and 1539 reactions. It has been successfully applied in combination with the soot model in previous studies of laminar ethylene/air counterflow flames in [45] and LES of a real aero-engine combustor [47].

4.2. Soot particle modeling

The soot particle model accounts for the evolution and dynamics of the solid particles in the flame, including their initial formation, particle interaction with the gas phase, and the interaction between multiple particles. In the S-EQMOM approach, developed in [22], particles are assumed to be spherical and characterized by their volume V, resulting in a volume-based univariate number density function (NDF) $n(x_i, t; V)$, which describes the particle population at each position x_i and time t in the flame. Since steady-state flames are investigated in this study, time dependencies are omitted below.

In the S-EQMOM, the evolution of the particle NDF, described by the population balance equation, is not solved directly but approximated by the evolution of its statistical moments m_k of the order k, defined as

$$m_k = \int_{V=V_{inception}}^{\infty} V^k n(x_i; V)\mathrm{d}V. \quad (5)$$

The transport equation describing the evolution of the kth moment is given by:

$$\frac{\partial m_k}{\partial t} + \frac{\partial}{\partial x_i}([u_i + u_{T,i}]m_k) = \dot{m}_k. \tag{6}$$

The soot particles follow the velocity of the gas phase u_i due to their low Stokes number. The velocity change due to thermophoretic effects $u_{T,i}$ is modeled by $u_{T,i} = -0.55\frac{\nu}{T}\frac{\partial T}{\partial x_i}$ including the local temperature T and the kinematic viscosity ν [48]. Diffusion effects are neglected due to the high Schmidt numbers of soot particles [49]. The right-hand side of Eq. (6) $\dot{m}_k$ represents the source terms of the moments due to interactions of the particles with the gas phase and particle–particle collisions. Their physical and chemical modeling is described as follows. Inception, i.e., the formation step of soot particles, is assumed to occur through the collision of two pyrene molecules [50], resulting in the formation of a particle with a volumetric size denoted as $V_{inception}$. The chemical surface growth by C_2H_2 is modeled according to the hydrogen-abstraction-C_2H_2-addition (HACA) mechanism [51], while OH and O_2 lead to particle oxidation [52]. The rate parameters for both processes are based on the work by Appel et al. [53]. PAH deposition onto the particle surface, also known as PAH-condensation, is described by the collision of particles with pyrene [50]. Collisions between multiple particles are assumed to result in coalescence, which is thus the sole coagulation process considered in this univariate model. Two collision kernels for the free molecular regime and the continuum regime are differentiated and a smooth transition between both regimes is achieved by applying a blending function [54]. The consumption of gas-phase species due to the described soot processes is considered in the species balance equations, establishing a coupling between the gas and soot particle phases.

To achieve the closure for the moment source terms $\dot{m}_k$, which rely on the distribution itself in the case of soot growth, oxidation, and particle–particle collisions, the S-EQMOM [22] is applied. S-EQMOM is based on the approach of the Extended Quadrature Method of Moments (EQMOM), which is described in the work of Yuan et al. [55]. Both methods employ multiple kernel density functions of a given geometric shape to describe the particle NDF, which may exhibit a complex and multimodal distribution shape. In contrast to the standard EQMOM, the S-EQMOM splits the volume-based NDF $n(V)$ into a sum of N_s sub-NDFs $n_{s_i}(V)$ leading to [22]:

$$n(V) = \sum_{j=1}^{N_s} n_{s_j}(V) \approx \sum_{j=1}^{N_s} w_{s_j}\delta_{\sigma_{s_j}}(V, V_{s_j}). \tag{7}$$

Each sub-NDF $n_{s_i}(V)$ is individually approximated by a geometric function $\delta_{\sigma_{s_i}}(V, V_{s_i})$ of a predefined shape. w_{s_i} represents the corresponding weights and V_{s_i} the node or inner coordinate positions. In contrast to the standard EQMOM, where the inversion is applied to the moments of the entire NDF, in S-EQMOM the inversion is performed for each sub-NDF individually and the NDF is reconstructed based on the sum of the sub-NDFs. Applying this strategy leads to a unique solution of the moment inversion and thus to enhanced numerical robustness and stability [22]. In this work, the NDF of the soot particles is approximated using three sub-NDFs, each described by gamma function distributions [56]. The shape parameters of each sub-NDF are reconstructed from three of their lower-order moments, resulting in a total of nine transported moments to represent the particle size distribution (PSD). Further details of the modeling approach can be found in the work of Salenbauch et al. [22], which has been applied both in laminar [22,45] and turbulent conditions [47,57,58].

5. Results

First, the numerical temperature profiles and gas-phase species mole fractions are compared with the experimental data to validate the simulation setup. Following this gas-phase validation, detailed investigations are carried out to understand the effect of ethanol at varying blending ratios on sooting characteristics and the individual soot formation processes.

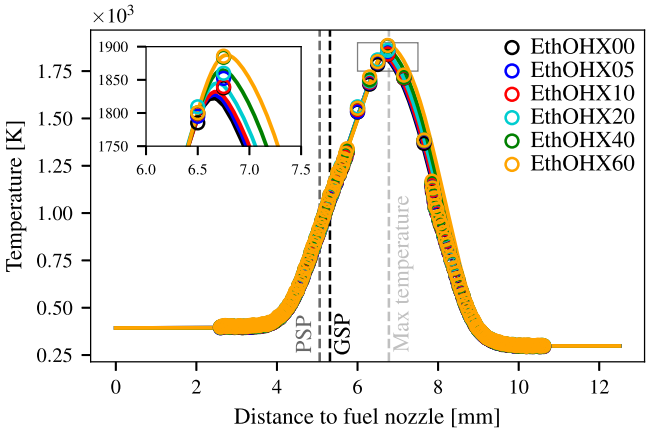

Fig. 1. Experimental (symbols) and simulated (lines) temperature profiles for varying ethanol content. Dashed vertical lines indicate the particle stagnation plane (PSP), gas-phase stagnation plane (GSP), and temperature peak location. The inset presents a close-up of the temperature peak region.

5.1. Gas-phase results

Fig. 1 shows the temperature profiles obtained from the simulations and their corresponding experimental data for varying amounts of ethanol in the fuel mixture, as a function of the distance from the fuel nozzle. The positions of the peak temperature, the gas-phase stagnation plane, and the particle stagnation plane from the simulations are indicated as vertical lines. The peak temperatures, which are also reported in Table 1, increase marginally with higher ethanol content, while all the maximum temperatures remain within a narrow range of 60 K. The reaction zones are located on the oxidizer side, causing the soot particles to form on the fuel rich side, i.e., on the left side of the flame temperature peak. Here, no significant differences in the temperature profiles can be observed. This consistency between the flames minimizes the effect of temperature and flame structure on flame chemistry, thereby isolating the influence of fuel chemical composition from other effects on gas-phase species and soot precursor formation.

The mole fraction profiles of selected combustion products and intermediate species obtained by the simulations are shown in Fig. 2 and compared with available experimental data for CO and H_2O. Increasing the ethanol content in the fuel mixture leads to an increase in CO, OH, and H_2O mole fractions. The oxygenation of the ethanol is the primary cause of these trends, as OH and H_2O are immediate products during the breakdown of the ethanol molecule [59,60]. Changes in OH-radical are especially relevant for the oxidation of soot particles. Overall, these simulation results closely reproduce the experimental trends both qualitatively and quantitatively, indicating that the main properties of the flames are well captured in the simulation.

To evaluate the influence of ethanol on the formation of soot precursor species, mole fraction profiles of acetylene (C_2H_2), naphthalene (A2), and pyrene (A4) are visualized in Fig. 3. Experimental data are available for C_2H_2 and A2. The C_2H_2 profile is almost unchanged at a lower ethanol content in the fuel mixture with non-monotonic behavior for the flame EthOHX10, while moderately increased acetylene mole fractions are observed at ethanol contents of 20 % and above. The simulations capture this trend, while slightly overpredicting the overall experimental values. A2 and A4 mole fraction peaks decrease with increasing ethanol content with an intermediate plateau for the A2 profile between EthOHX10 and EthOHX20. Therefore, both PAH species show an overall inverse trend compared to C_2H_2 with increasing ethanol content in the fuel. Close to the particle stagnation plane, an increase in the A2 and A4 mole fraction profiles can be observed for the 5 % ethanol flame compared to the neat gasoline flame. This behavior can be explained by the increased reactivity associated with small

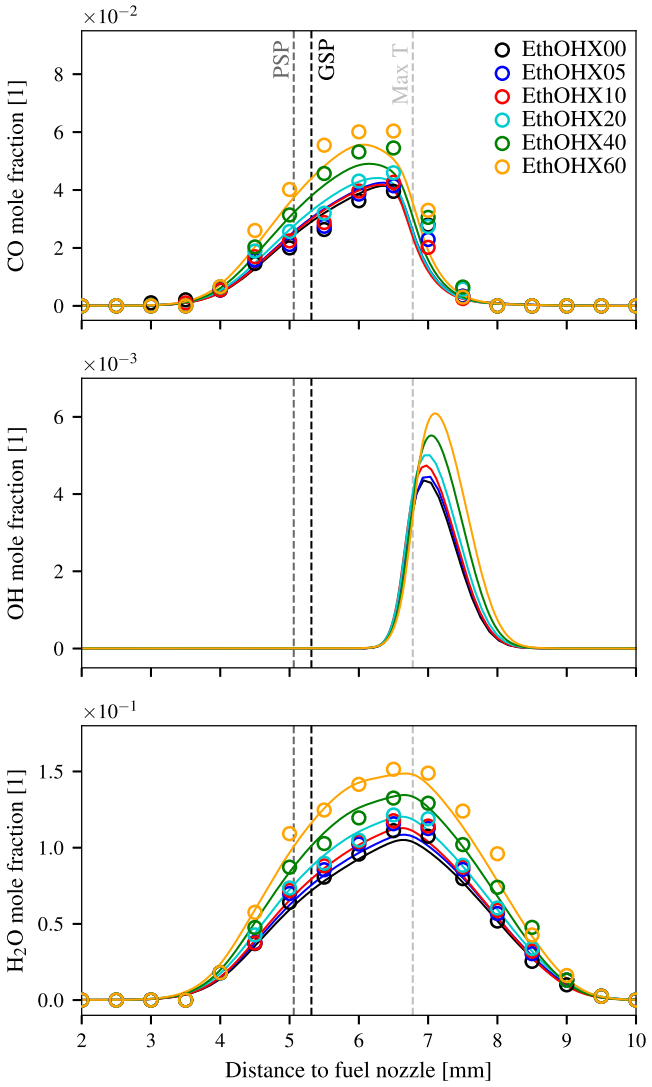

Fig. 2. Experimental (symbols) and simulated (lines) mole fractions of CO (top), OH (middle), and H_2O (bottom) for varying ethanol content.

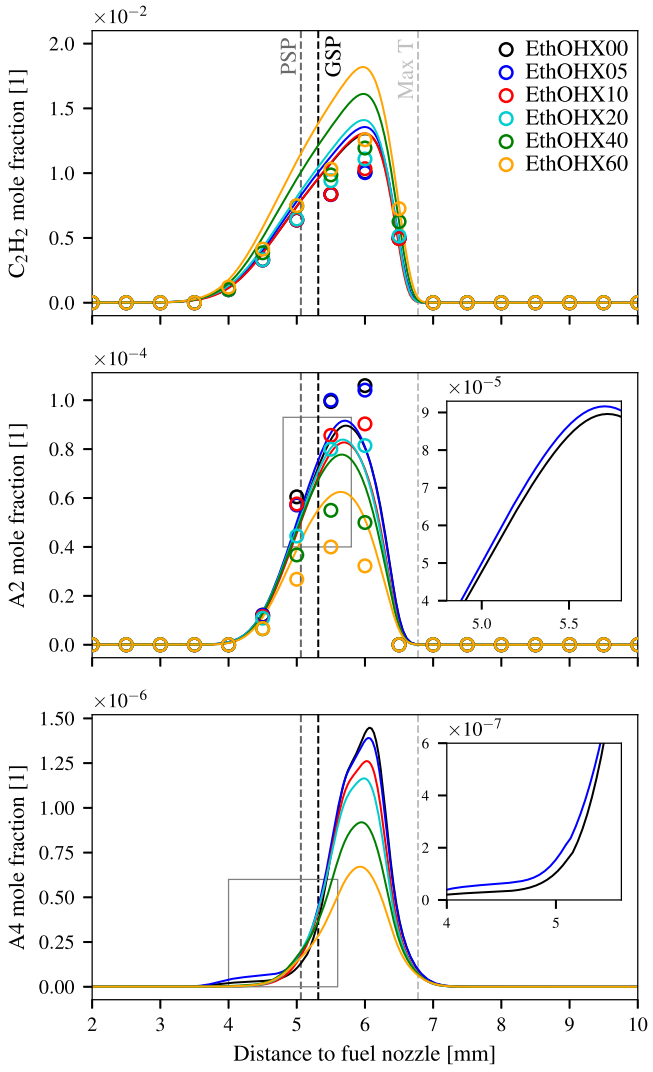

Fig. 3. Experimental (symbols) and simulated (lines) mole fractions of C_2H_2 (top), A2 (middle), and A4 (bottom) for varying ethanol content. The insets show the A2 and A4 mole fraction profile of the two flames EthOHX00 and EthOHX05 near the particle stagnation plane.

amounts of ethanol, which enhances the radical pool generated during fuel decomposition, consistently with the results in [11]. At higher ethanol contents, fuel oxidation resulting from added oxygen and accompanying dilution effects becomes dominant, thereby reducing PAH formation again. The simulation accurately captures the experimental data for A2; however, it exhibits a reduced sensitivity to variations in ethanol content. A higher sensitivity is predicted by the modeling for the A4 mole fraction as shown in Fig. 3. The reduction of C_7H_8 in the fuel mixture of the ethanol flames, as noted in Table 1, is unlikely to be the sole reason for the reduction of larger aromatics, because the reduction of larger PAHs, such as A4, exceeds the changes of C_7H_8 in the fuel mixture. Therefore, adding ethanol to the fuel mixture not only dilutes the amount of C_7H_8, but also appears to actively alter PAH formation processes, thereby affecting the initial soot formation step.

5.2. Soot evolution

Fig. 4 shows the experimental and modeled soot volume fraction profiles for the various blends of ethanol in the fuel. The soot particles are formed and grow in the fuel-rich side of the reaction layer, where large PAHs and acetylene are present. Soot particles are then transported toward the fuel nozzle and surpass the gas-phase stagnation plane (GSP) due to thermophoresis, resulting in a soot formation flame structure. The simulations correctly predict the soot inception and growth region, the stagnation plane location as well as the qualitative trend of the experimental data. However, the computed profiles underestimate the experimental results by almost a factor of ten. Both experimental and numerical results indicate a notable reduction in soot volume fraction with increasing amount of ethanol. A slight increase in soot volume fraction occurs only when 5 % ethanol is blended, which represents an exception to this trend. This particular effect observed in the experiments is captured by the numerical model. Similar behavior with an increase in particle formation at lower blending ratios has been observed for ethanol [13,17–19] and other oxygenated fuels in the literature, especially for nanoparticle formation [61].

The normalized peak values of the simulated soot volume fraction profiles and the experimental data are summarized in Fig. 5 to demonstrate the quantitative reduction in the soot volume fraction for different amounts of ethanol in the fuel mixture. Both the experimental and simulation results exhibit their maximum soot volume fraction at 5 % ethanol, which is used to normalize the data. Slightly smaller values of the normalized soot volume fraction can be observed in both experiments and simulation at 0 % ethanol, while a larger, monotonic reduction is obtained starting from 10 % ethanol concentration and

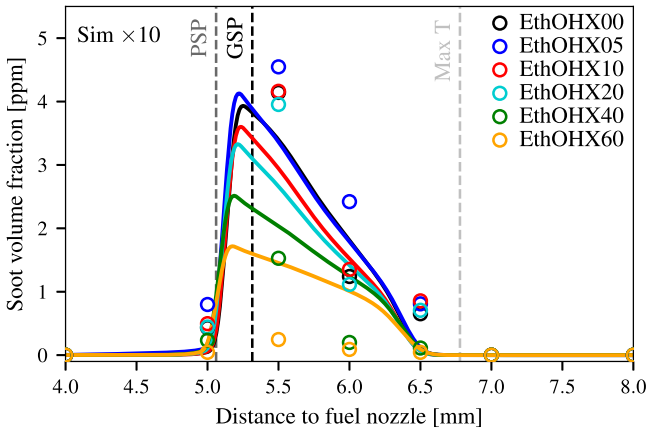

Fig. 4. Experimental (symbols) and simulated (lines) soot volume fraction profiles for varying ethanol contents.

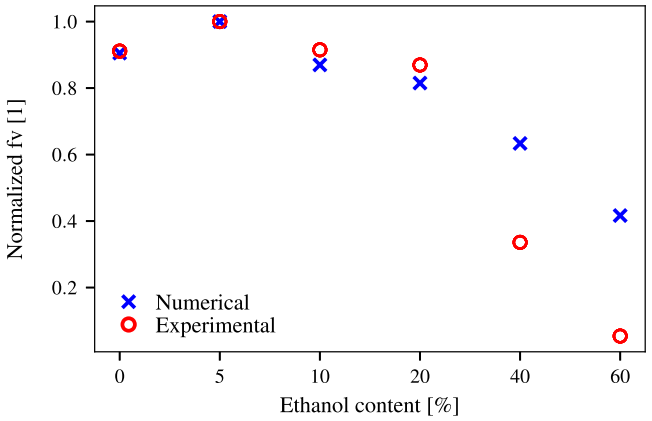

Fig. 5. Normalized soot volume fraction peak values of experimental data and simulations for varying ethanol content.

beyond. The numerical predictions from 0 % up to 20 % ethanol concentration are quantitatively well captured by the simulations. However, at the highest ethanol concentration investigated, the measured soot volume fraction decreases of 95 %, while the simulation predicts only a 60 % reduction. The gas-phase kinetics of soot precursors may partially contribute to this discrepancy. As discussed in Section 5.1, the simulated C_2H_2 mole fraction profiles shown in Fig. 3 exhibit a slight overprediction compared to the experimental data. This deviation may lead to a slight overestimation of the C_2H_2-related HACA process across all flames investigated, regardless of the ethanol content. A systematic overprediction of the HACA contribution tends to diminish the relative influence of other soot processes, thereby reducing the sensitivity of the soot volume fraction to variations in ethanol content. Additionally, although the A2 mole fraction is well captured, a reduced sensitivity of its profiles to variations in the ethanol blending ratio in the fuel can be observed in Fig. 3. This leads to uncertainties in subsequent PAH growth pathways and PAH-related soot processes, which in turn are assumed to be less sensitive to changes in ethanol content. Both deviations may reduce the sensitivity of the simulated soot volume fraction to high ethanol content.

To better understand these effects and clarify the predominant mechanism of ethanol blending on soot formation pathways, the contribution to soot particulate matter from each individual soot process such as inception, surface growth through the HACA-mechanism, surface growth through PAH-deposition (condensation), and oxidation is presented in Fig. 6. The data reveal that the maximum rates of inception of young soot particles, as well as the subsequent growth rates by both the HACA-mechanism and PAH-deposition, systematically decrease as the ethanol fraction in the fuel blend is increased. Additionally, both HACA and oxidation rates are active in a narrow spatial region, between 6 and 6.5 mm, compared to the broader region where soot is present and nucleation and condensation occur, from 5 to 6.5 mm. The observed trends in nucleation and PAH-deposition can be attributed to a general decrease in the A4 mole fraction peak, the sole species considered for the modeling of these soot processes. This trend is present across the flame except close to the particle stagnation plane, as shown in Fig. 3.

The HACA source term depends on both C_2H_2 concentration and the particle size distribution itself. Therefore, since C_2H_2 is formed in larger amounts at higher ethanol concentration (see Fig. 3), the reduction of HACA source term may be attributed to a lower total active particle surface area available to interact with C_2H_2 at higher ethanol contents. Inception and condensation are strongly sensitive to ethanol content, while the variation of the HACA-mechanism is comparatively moderate. The magnitude of soot oxidation also decreases with increasing ethanol content in the fuel mixture. As a result, oxidation does not contribute an additional soot reduction effect for increasing ethanol blending compared to the flames without (EthOHX00). The trend of the absolute value of soot oxidation does not correlate with the changes in the OH profiles shown in Fig. 2. Similarly to the HACA-mechanism, the reduction in oxidation rate can be explained by a less active surface on the soot particles at higher ethanol content in the fuel mixture. Furthermore, OH is present primarily in a region between 6.5 mm and 8.0 mm, while soot particles begin to form closer to the fuel nozzle, for a distance lower than 6.5 mm. These processes suggest that PAHs and PAH-based soot processes are the dominant factors influencing the effect of ethanol on soot formation in the flames studied, rather than oxidation or the HACA-mechanism. Therefore, the overprediction of naphthalene (A2) observed at 40 and 60 % ethanol blends in Fig. 3 might cause a higher concentration of larger PAHs as pyrene (A4), consequently resulting in the overestimation of soot formation observed in Figs. 4 and 5. The peak soot volume fraction shows a non-monotonic dependency on ethanol content, with an intermediate maximum at 5 % ethanol shown in Fig. 5. This behavior contradicts the monotonic decrease observed for the absolute peak values of all four soot formation processes plotted in Fig. 6, as the ethanol fraction is increased. The flame containing 5 % ethanol shows slightly higher nucleation and condensation rates in the vicinity of the stagnation plane, where particle residence times are longest. This can be directly linked to the A4 species profile shown in Fig. 3. At a $HAB = 5$ mm, the mole fraction of A4 is noticeably greater for the 5 %-ethanol flame than for the neat gasoline case, indicating that the enhanced nucleation/condensation at this location is responsible for the intermediate soot volume fraction maximum. Here, slight variations in the processes have time to accumulate, which ultimately explains the non-monotonic effects.

5.3. Particle size distribution

The PSDs of all investigated flames are numerically and experimentally analyzed to determine the effects of ethanol blending on the formation of both small and large soot particles. Fig. 7 presents the normalized particle size distributions for both the experimental and numerical data at axial distance $HAB = 5.5$ mm, corresponding approximately to the peak soot volume fraction location within the flames. Each distribution is individually normalized either by the maximum number concentration of their second mode or by the corresponding experimental data, respectively. The results are presented here on a linear scale to clearly highlight the effect of ethanol on the second PSD mode. The correspondent log-scale plot is provided in the appendix. Overall, both experimental and numerical results indicate a decrease in particle diameter at their number concentration peaks with increasing ethanol content. However, this trend is different for lower ethanol content: the EthOHX05 flame exhibits the largest particle diameters, following the

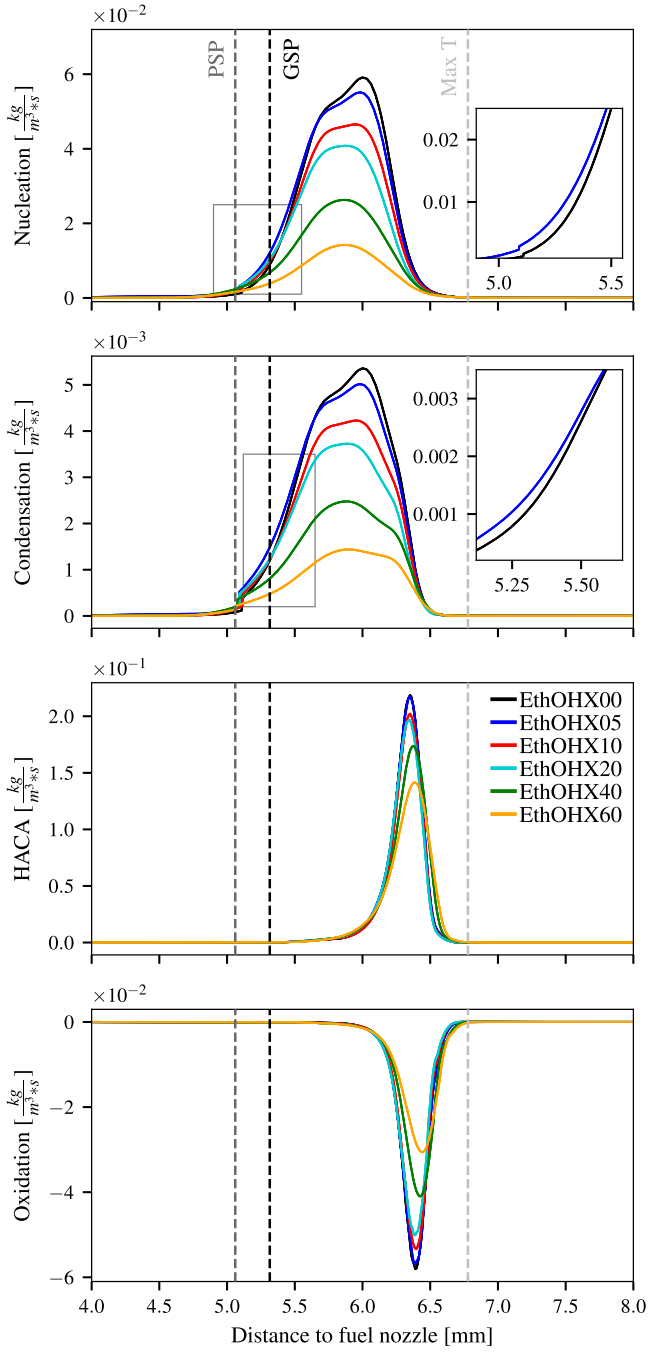

Fig. 6. Computed source terms of the individual soot processes for varying ethanol content: nucleation, PAH-deposition, HACA-mechanism, and soot oxidation (from top to bottom). Insets highlight the source terms for the EthOHX00 and EthOHX05 flames near the particle stagnation plane.

trend of soot volume fraction for increasing ethanol content. Quantitatively, the peak diameter in the experimental results varies between $7\,\text{nm} \leq d_p \leq 54\,\text{nm}$ and therefore features larger sensitivity than the numerical results, which have peak diameter changes of the second mode between $35\,\text{nm} \leq d_p \leq 50\,\text{nm}$. This trend remains significant even when the experimental uncertainty of less than 20 % is taken into account. The numerical results additionally indicate the formation of smaller particles with particle diameters $d_p \leq 5\,\text{nm}$, representing the inception mode. These nascent particles exhibit negligible absorption at the near-infrared laser wavelength used for 2C-TiRe-LII [20]. As a result, they remain undetected in the experiments.

Nevertheless, the particle size distributions obtained by 2C-TiRe-LII are in good agreement with the nucleation mode particle sizes reported by Maricq et al. [62] for ethanol/gasoline coflow diffusion flames, indicating that the primary particle sizes are of the same order of magnitude as those in the counterflow diffusion flames investigated here. Frenzel et al. [12] observed smaller count median diameters in premixed iso-octane/ethanol flames without aromatics, but when comparing flames with similar soot volume fractions, the reported values are consistent with the present results. Unfortunately, further validation data are not available.

To further investigate nanoparticle formation, Fig. 8 displays the experimental and modeled PSDs at three different axial positions within the flame on logarithmic scales. The data at $HAB = 5.5\,\text{mm}$ corresponds to the data of Fig. 7. Additional PSDs are provided for positions on the fuel side of the particle stagnation plane ($HAB = 5.0\,\text{mm}$) and closer to the flame front ($HAB = 6.0\,\text{mm}$). At $HAB = 5.0\,\text{mm}$, both the experimental and the modeling results mainly indicate the presence of particles with a diameter smaller than $d_p = 10\,\text{nm}$. The simulation results show the formation of a second mode with particle diameters in the range of $10\,\text{nm} \leq d \leq 20\,\text{nm}$, hence the transition from unimodal to bimodal PSDs. The largest particles are formed in the EthOHX05 flame while no clear trend is observed for other ethanol blending ratios at this position in the flame. Afterwards, the soot particles are transported towards the particle stagnation plane at approximately $HAB = 5.1\,\text{mm}$ limiting further particle evolution on the fuel nozzle side of the particle stagnation plane.

The PSDs at $HAB = 6.0\,\text{mm}$ represent an early stage in the particle maturation process. This stage occurs after the initial inception at higher $HABs$, near the flame front, and precedes the convective transport of the particles to $HAB = 5.5\,\text{mm}$, shown in the center column of Fig. 8. Ultimately, the particles reach the peak soot volume fraction position on the oxidizer side of the particle stagnation plane. Therefore, at $HAB = 6.0\,\text{mm}$, the PSDs exhibit particles with smaller peak diameters and higher number density than at $HAB = 5.5\,\text{mm}$. However, they follow the trends observed for varying ethanol blending ratios in Fig. 7. While experimental data only proves the presence of larger particles at these positions, simulation results also indicate a significant decrease in the number of smaller particles at ethanol contents above 10 vol%.

6. Conclusion

In this study, the effects of ethanol blending on the sooting behavior of non-premixed gasoline surrogate flames are investigated. Counterflow diffusion flames under constant conditions of strain, flame position, and carbon stream, but with varying amounts of ethanol, are studied combining experimental data with detailed numerical simulations. Detailed kinetics combined with the S-EQMOM soot modeling approach are employed to provide a deeper insight into the underlying soot formation processes. The results show that small additions of ethanol increase the amount of soot formed, while higher amounts of ethanol significantly reduce soot particulate matter. This non-monotonic trend, featuring a maximum soot volume fraction at approx. 5 vol% ethanol and a noticeable soot reduction at intermediate ethanol contents, is well captured by the model, although it quantitatively underpredicts the soot reduction at higher ethanol levels. Further analysis indicates that soot inception, condensation, and HACA-mechanism are reduced at higher ethanol ratios, while the processes most sensitive to the ethanol content are those governed by the PAH concentrations. Although both the absolute HACA-process and soot oxidation decrease with increasing ethanol blending, the corresponding gas-phase species concentrations (C_2H_2 and OH) exhibit opposite trends. These findings suggest that the inception and condensation mechanisms are the main limiting factors of the soot formation process when ethanol is added, leading to the observed soot reduction effects under the investigated non-premixed conditions. Additionally, the investigated particle size distribution primarily shows a reduction in peak diameter for larger particles and a reduction in number

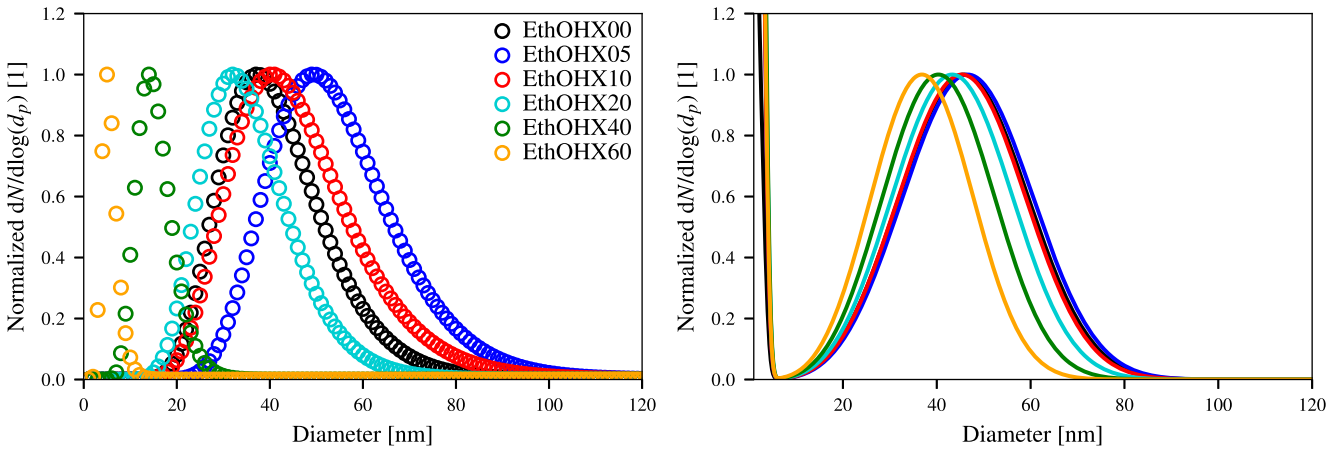

Fig. 7. Normalized particle size distribution of experimental data (left) and simulation results (right) at $HAB = 5.5\,\text{mm}$. All distributions are normalized to the peak particle concentration, while the corresponding value of the second PSD mode is used for the simulation results.

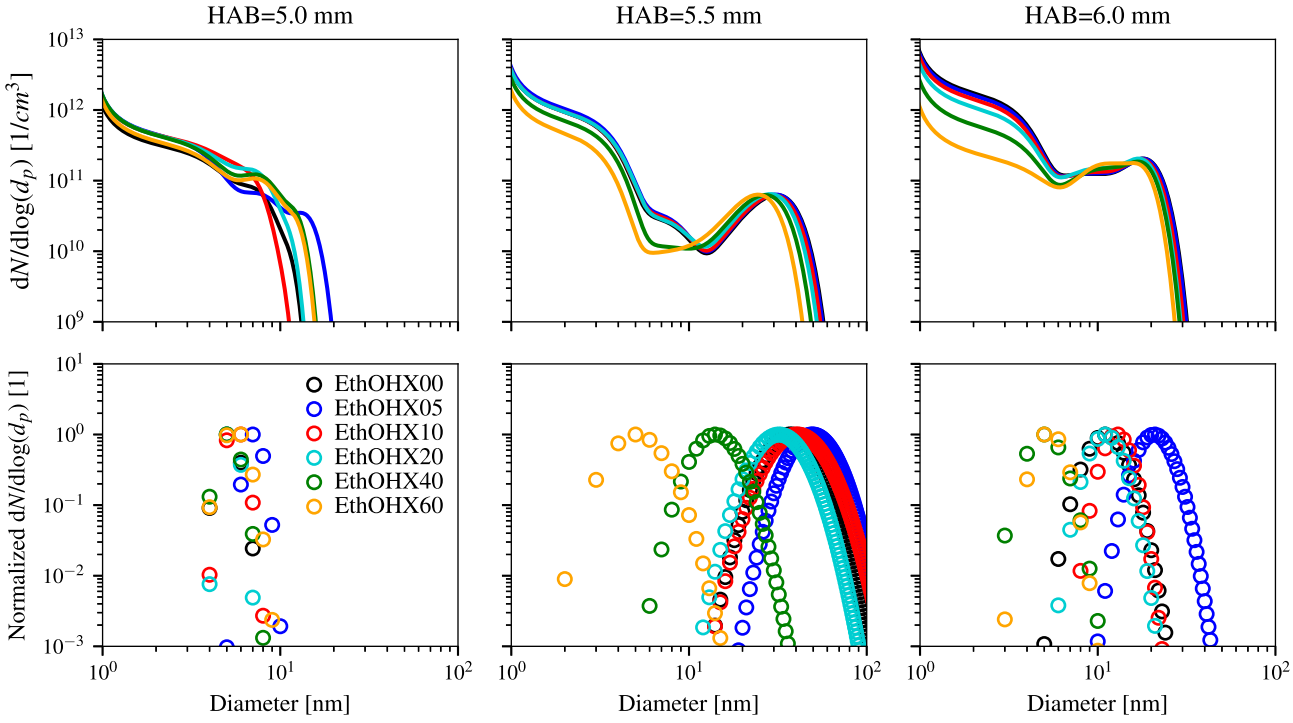

Fig. 8. Normalized particle size distribution for varying ethanol content at $HAB = 5.0\,\text{mm}$ (left column), $HAB = 5.5\,\text{mm}$ (middle column), and $HAB = 6.0\,\text{mm}$ (right column). Experimental results (bottom row) are normalized to the peak number, whereas simulation results (top row) are in absolute numbers.

concentration for smaller particles. These effects occur at intermediate and higher blending ratios, while low ethanol amounts increase the particle diameter. This result is of significant importance, as it contributes to a deeper understanding of the effects of ethanol fuel blends not only on soot volume fraction but also on the size of the produced particles. In particular, quantifying the impact of ethanol blending on the production of fine particles, which are challenging to detect experimentally, provide valuable input for future assessment on the potential effects on local air quality and human health.

Open Access Disclosure Statement

The Combustion Institute has provided financial sponsorship to make the special issue entitled “Women in Combustion Part 2” open access and had no influence or involvement over the review or approval of any content.

CRediT authorship contribution statement

Fenja Ahrendt: Writing – original draft, Numerical Investigation, Data curation. **Robert Schmitz:** Writing – original draft, Supervision, Conceptualization. **Fabian P. Hagen:** Writing – review & editing, Experimental Investigation, Conceptualization. **Petros Vlavakis:** Writing – review & editing, Experimental Investigation. **Dimosthenis Trimis:** Writing – review & editing, Supervision, Funding acquisition, Conceptualization. **Federica Ferraro:** Writing – review & editing, Supervision, Funding acquisition, Conceptualization.

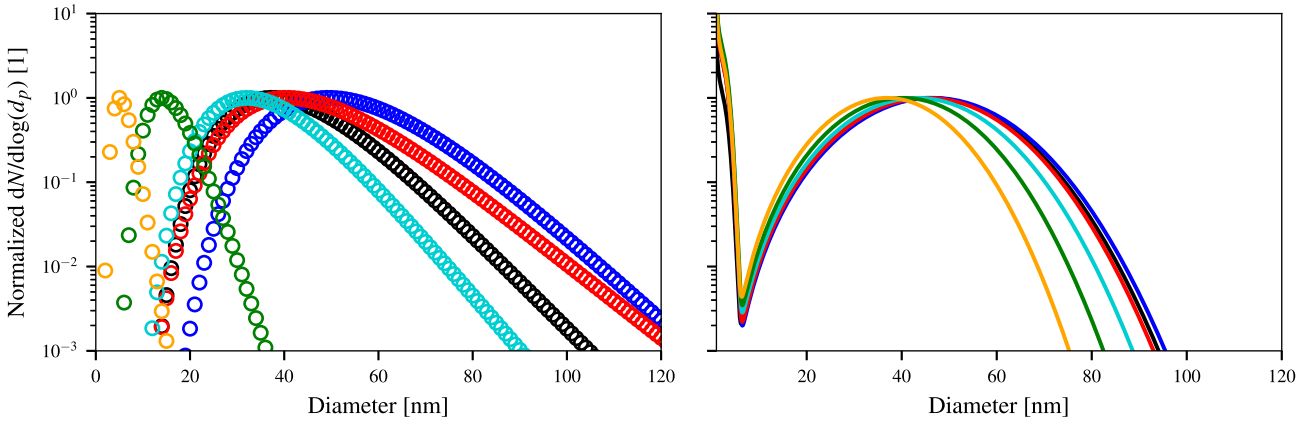

Fig. A.1. Normalized PSD of experimental data (left) and simulation results (right) at $HAB = 5.5\,\text{mm}$. All distributions are normalized to the peak number of their first (experiments) or second mode (simulations), respectively.

Declaration of competing interest

The authors declare that they have no known competing financial interests or personal relationships that could have appeared to influence the work reported in this paper.

Acknowledgments

This work is funded by the Deutsche Forschungsgemeinschaft (DFG, German Research Foundation) under Germany's Excellence Strategy—EXC 2163/1- Sustainable and Energy Efficient Aviation, Germany—Project-ID 390881007. Additionally, the research contributes to the Helmholtz Association's MTET program, Resource and Energy Efficiency, Anthropogenic Carbon Cycle (38.05.01). We thank Prof. C. Hasse (TU Darmstadt) for providing the ULF solver and Prof. M. Sirignano (Univ. Napoli Federico II) for the fruitful discussion.

Appendix. PSDs on logarithmic scale

To support the analysis of the effects of ethanol blending on the formation of both nanoparticles and larger soot particles, the particle size distribution results presented in Fig. 7 are also shown on a logarithmic scale in Fig. A.1.

Data availability

Data will be made available on request.

References

[1] Ritchie H, Rosado P, Roser M. CO_2 and greenhouse gas emissions. 2023, Our World in Data. Retrieved from: https://ourworldindata.org/co2-and-greenhouse-gas-emissions.

[2] Cherwoo L, Gupta I, Flora G, Verma R, Kapil M, Arya SK, Ravindran B, Khoo KS, Bhatia SK, Chang SW, Ngamcharussrivichai C, Ashokkumar V. Biofuels an alternative to traditional fossil fuels: A comprehensive review. Sustain Energy Technol Assess 2023;60:103503. http://dx.doi.org/10.1016/j.seta.2023.103503.

[3] Kohse-Höinghaus K, Oßwald P, Cool TA, Kasper T, Hansen N, Qi F, Westbrook CK, Westmoreland PR. Biofuel combustion chemistry: from ethanol to biodiesel. Angew Chem 2010;49(21):3572–97. http://dx.doi.org/10.1002/anie.200905335.

[4] Battin-Leclerc F, Curran H, Faravelli T, Glaude PA. Specificities related to detailed kinetic models for the combustion of oxygenated fuels components. In: Battin-Leclerc F, Simmie JM, Blurock E, editors. Cleaner combustion. London: Springer London; 2013, p. 93–109. http://dx.doi.org/10.1007/978-1-4471-5307-8_4.

[5] Lemaire R, Therssen E, Desgroux P. Effect of ethanol addition in gasoline and gasoline–surrogate on soot formation in turbulent spray flames. Fuel 2010;89(12):3952–9. http://dx.doi.org/10.1016/j.fuel.2010.06.031.

[6] Tan YR, Salamanca M, Akroyd J, Kraft M. How do the oxygenated functional groups in ether, carbonate and alcohol affect soot formation in jet A2 diffusion flames. Combust Flame 2022;243:111849. http://dx.doi.org/10.1016/j.combustflame.2021.111849.

[7] Chen L, Hu X, Wang J, Yu Y. Impacts of alternative fuels on morphological and nanostructural characteristics of soot emissions from an aviation piston engine. Environ Sci Technol 2019;53(8):4667–74. http://dx.doi.org/10.1021/acs.est.9b01059.

[8] Kennedy IM. The health effects of combustion-generated aerosols. Proc Combust Inst 2007;31(2):2757–70. http://dx.doi.org/10.1016/j.proci.2006.08.116.

[9] Yan F, Xu L, Wang Y, Park S, Sarathy SM, Chung SH. On the opposing effects of methanol and ethanol addition on PAH and soot formation in ethylene counterflow diffusion flames. Combust Flame 2019;202:228–42. http://dx.doi.org/10.1016/j.combustflame.2019.01.020.

[10] Salamanca M, Sirignano M, Commodo M, Minutolo P, D'Anna A. The effect of ethanol on the particle size distributions in ethylene premixed flames. Exp Therm Fluid Sci 2012;43:71–5. http://dx.doi.org/10.1016/j.expthermflusci.2012.04.006.

[11] Salamanca M, Sirignano M, D'Anna A. Particulate formation in premixed and counter-flow diffusion ethylene/ethanol flames. Energy & Fuels 2012;26(10):6144–52. http://dx.doi.org/10.1021/ef301081q.

[12] Frenzel I, Krause H, Trimis D. Study on the influence of ethanol and butanol addition on soot formation in iso-octane flames. Energy Procedia 2017;120:721–8. http://dx.doi.org/10.1016/j.egypro.2017.07.203.

[13] Lyu Z, Cen L, Qian Y, Yan T, Zhou D, Lu X. Experimental and numerical investigation of the synergistic effect on soot formation in ethanol/n-heptane laminar diffusion flames at elevated pressures. Combust Flame. 2024;266:113561. http://dx.doi.org/10.1016/j.combustflame.2024.113561.

[14] Koegl M, Hofbeck B, Will S, Zigan L. Investigation of soot formation and oxidation of ethanol and butanol fuel blends in a DISI engine at different exhaust gas recirculation rates. Appl Energy 2018;209:426–34. http://dx.doi.org/10.1016/j.apenergy.2017.11.034.

[15] Do H-Q, Therssen E, Sood K, Giarracca-Mehl L, Lefort B, Tran L-S, Mercier X. Characterization of the impact of ethanol on the formation of soot particles in gasoline turbulent diffusion flames. Proc Combust Inst 2024;40(1–4):105468. http://dx.doi.org/10.1016/j.proci.2024.105468.

[16] McNesby KL, Miziolek AW, Nguyen T, Delucia FC, Reed Skaggs R, Litzinger TA. Experimental and computational studies of oxidizer and fuel side addition of ethanol to opposed flow air/ethylene flames. Combust Flame 2005;142(4):413–27. http://dx.doi.org/10.1016/j.combustflame.2005.04.003.

[17] Esposito V, Sirignano M. Effect of strain rate on nanoparticles and soot in counterflow flames of ethylene/ethanol and ethylene/OME3. Fuel 2025;379:133094. http://dx.doi.org/10.1016/j.fuel.2024.133094.

[18] McEnally CS, Pfefferle LD. The effects of dimethyl ether and ethanol on benzene and soot formation in ethylene nonpremixed flames. Proc Combust Inst 2007;31(1):603–10. http://dx.doi.org/10.1016/j.proci.2006.07.005.

[19] Yang SS, Gülder ÖL. Sooting characteristics of ethanol-ethylene blends in laminar coflow diffusion flames up to 10 bar. Combust Flame 2021;225:39–47. http://dx.doi.org/10.1016/j.combustflame.2020.10.032.

[20] Hagen FP, Vlavakis P, Seitz M, Klövekorn T, Bockhorn H, Suntz R, Trimis D. Soot nanoparticle sizing in counterflow flames using in-situ particle sampling and differential mobility analysis verified with two-colour time-resolved laser-induced incandescence. Proc Combust Inst 2023;39(1):1119–28. http://dx.doi.org/10.1016/j.proci.2022.07.253.

[21] Hagen FP, Vlavakis P, Bockhorn H, Suntz R, Trimis D. From molecular to sub-μ m scale: The interplay of precursor concentrations, primary particle size, and carbon nanostructure during soot formation in counter-flow diffusion flames. Combust Flame 2023;258:112729. http://dx.doi.org/10.1016/j.combustflame.2023.112729.

[22] Salenbauch S, Hasse C, Vanni M, Marchisio DL. A numerically robust method of moments with number density function reconstruction and its application to soot formation, growth and oxidation. J Aerosol Sci 2019;128:34–49. http://dx.doi.org/10.1016/j.jaerosci.2018.11.009.

[23] Seshadri K, Williams F. Laminar flow between parallel plates with injection of a reactant at high Reynolds number. Int J Heat Mass Transfer 1978;21:251–3. http://dx.doi.org/10.1016/0017-9310(78)90230-2.

[24] Niemann U, Seshadri K, Williams FA. Accuracies of laminar counterflow flame experiments. Combust Flame 2015;162(4):1540–9. http://dx.doi.org/10.1016/j.combustflame.2014.11.021.

[25] Vlavakis P, Hagen FP, Loukou A, Trimis D. Soot formation in iso-octane counterflow diffusion flames. Combust Flame 2025;282:114513. http://dx.doi.org/10.1016/j.combustflame.2025.114513.

[26] Saggese C, Whitesides R, Wagnon SW, Chatterjee T, Hagen FP, Vlavakis P, Schraud N, Trimis D. Soot formation and precursor chemistry in counterflow flames of aviation fuel surrogates. Proc Combust Inst 2025;41:105816. http://dx.doi.org/10.1016/j.proci.2025.105816.

[27] Khare R, Vlavakis P, Langenthal TV, Loukou A, Khosravi M, Kramer U, Trimis D. Experimental investigation of the effect of hydrogen addition on the sooting limit and structure of methane/air laminar counterflow diffusion flames. Fuel 2022;324:124506. http://dx.doi.org/10.1016/j.fuel.2022.124506.

[28] Shaddix CR. Correcting thermocouple measurements for radiation loss: A critical review. In: Proceedings of the 33rd national heat transfer conference nHTC'99. Sandia National Labs., Livermore, CA (US), American Society of Mechanical Engineers, New York, NY (US); 1999, p. 282–91, URL https://www.osti.gov/biblio/20002672.

[29] Carbone F, Gomez A. The structure of toluene-doped counterflow gaseous diffusion flames. Combust Flame 2012;159(10):3040–55. http://dx.doi.org/10.1016/j.combustflame.2012.05.003.

[30] Valencia-López AM, Bustamante F, Loukou A, Stelzner B, Trimis D, Frenklach M, Slavinskaya NA. Effect of benzene doping on soot precursors formation in non-premixed flames of producer gas (PG). Combust Flame. 2019;207:265–80. http://dx.doi.org/10.1016/j.combustflame.2019.05.044.

[31] Liu F, Stagg BJ, Snelling DR, Smallwood GJ. Effects of primary soot particle size distribution on the temperature of soot particles heated by a nanosecond pulsed laser in an atmospheric laminar diffusion flame. Int J Heat Mass Transfer 2006;49(3):777–88. http://dx.doi.org/10.1016/j.ijheatmasstransfer.2005.07.041.

[32] Bladh H, Johnsson J, Olofsson N-E, Bohlin A, Bengtsson P-E. Optical soot characterization using two-color laser-induced incandescence (2C-LII) in the soot growth region of a premixed flat flame. Proc Combust Inst 2011;33(1):641–8. http://dx.doi.org/10.1016/j.proci.2010.06.166.

[33] Hagen FP, Suntz R, Bockhorn H, Trimis D. Dual-pulse laser-induced incandescence to quantify carbon nanostructure and related soot particle properties in transient flows – concept and exploratory study. Combust Flame 2022;243:112020. http://dx.doi.org/10.1016/j.combustflame.2022.112020, A dedication to Professor Katharina Kohse-Höinghaus.

[34] Török S, Mannazhi M, Bengtsson P-E. Laser-induced incandescence (2 λ and 2C) for estimating absorption efficiency of differently matured soot. Appl Phys B 2021;127(7):96. http://dx.doi.org/10.1007/s00340-021-07638-1.

[35] Olofsson N-E, Simonsson J, Török S, Bladh H, Bengtsson P-E. Evolution of properties for aging soot in premixed flat flames studied by laser-induced incandescence and elastic light scattering. Appl Phys B 2015;119(4):669–83. http://dx.doi.org/10.1007/s00340-015-6067-3.

[36] Desgroux P, Lamoureux N, Faccinetto A. Combining performances of E (m)-corrected LII and absorption for in situ measurements of the volume fraction of 2–4 nm soot particles.. J Aerosol Sci 2024;179:106385. http://dx.doi.org/10.1016/j.jaerosci.2024.106385.

[37] Snelling DR, Liu F, Smallwood GJ, Gülder ÖL. Determination of the soot absorption function and thermal accommodation coefficient using low-fluence LII in a laminar coflow ethylene diffusion flame. Combust Flame 2004;136(1):180–90. http://dx.doi.org/10.1016/j.combustflame.2003.09.013.

[38] Michelsen H, Schulz C, Smallwood G, Will S. Laser-induced incandescence: Particulate diagnostics for combustion, atmospheric, and industrial applications. Prog Energy Combust Sci 2015;51:2–48. http://dx.doi.org/10.1016/j.pecs.2015.07.001.

[39] Bauer FJ, Daun KJ, Huber FJT, Will S. Can soot primary particle size distributions be determined using laser-induced incandescence? Appl Phys B 2019;125(6):109. http://dx.doi.org/10.1007/s00340-019-7219-7.

[40] Kock BF, Tribalet B, Schulz C, Roth P. Two-color time-resolved LII applied to soot particle sizing in the cylinder of a diesel engine. Combust Flame 2006;147(1):79–92. http://dx.doi.org/10.1016/j.combustflame.2006.07.009.

[41] Hadef R, Geigle KP, Meier W, Aigner M. Soot characterization with laser-induced incandescence applied to a laminar premixed ethylene–air flame. Int J Therm Sci 2010;49(8):1457–67. http://dx.doi.org/10.1016/j.ijthermalsci.2010.02.014.

[42] Zschutschke A, Messig D, Scholtissek A, Hasse C. Universal Laminar Flame Solver (ULF). 2017, http://dx.doi.org/10.6084/M9.FIGSHARE.5119855.V2, 4893736 Bytes.

[43] Ramirez Hernandez A, Kathrotia T, Methling T, Braun-Unkhoff M, Riedel U. Reaction model development of selected aromatics as relevant molecules of a kerosene surrogate—the importance of *m* -Xylene Within the combustion of 1,3,5-trimethylbenzene. J Eng Gas Turbine. Power 2022;144(2):021002. http://dx.doi.org/10.1115/1.4052206.

[44] Ramirez Hernandez AR, Kathrotia T, Methling T, Braun-Unkhoff M, Riedel U. An upgraded chemical kinetic mechanism for *Iso* -octane oxidation: prediction of polyaromatics formation in laminar counterflow diffusion flames. J Eng Gas Turbine. Power 2023;145(6):061006. http://dx.doi.org/10.1115/1.4056096.

[45] Kalbhor A, Schmitz R, Ramirez A, Vlavakis P, Hagen FP, Ferraro F, Braun-Unkhoff M, Kathrotia T, Riedel U, Trimis D, Van Oijen J, Hasse C, Mira D. Experimental and numerical investigation on soot formation and evolution of particle size distribution in laminar counterflow ethylene flames. Combust Flame. 2024;260:113220. http://dx.doi.org/10.1016/j.combustflame.2023.113220.

[46] Salenbauch S, Cuoci A, Frassoldati A, Saggese C, Faravelli T, Hasse C. Modeling soot formation in premixed flames using an extended conditional quadrature method of moments. Combust Flame 2015;162(6):2529–43. http://dx.doi.org/10.1016/j.combustflame.2015.03.002.

[47] Koob P, Ferraro F, Nicolai H, Eggels R, Staufer M, Hasse C. Large eddy simulation of soot formation in a real aero-engine combustor using tabulated chemistry and a quadrature-based method of moments. J Eng Gas Turbines Power 2024;146(1):1–8. http://dx.doi.org/10.1115/1.4063376.

[48] Friedlander SK. Smoke, dust, and haze: Fundamentals of aerosol dynamics, In: Topics in chemical engineering, second ed.. New York: Oxford University Press; 2000.

[49] Bisetti F, Blanquart G, Mueller ME, Pitsch H. On the formation and early evolution of soot in turbulent nonpremixed flames. Combust Flame 2012;159(1):317–35. http://dx.doi.org/10.1016/j.combustflame.2011.05.021.

[50] Balthasar M, Kraft M. A stochastic approach to calculate the particle size distribution function of soot particles in laminar premixed flames. Combust Flame. 2003;133(3):289–98. http://dx.doi.org/10.1016/S0010-2180(03)00003-8.

[51] Frenklach M, Wang H. Detailed modeling of soot particle nucleation and growth. Symp Combust Proc 1991;23(1):1559–66. http://dx.doi.org/10.1016/S0082-0784(06)80426-1.

[52] Frenklach M, Wang H. Detailed mechanism and modeling of soot particle formation. In: Bockhorn H, editor. Soot formation in combustion. Berlin, Heidelberg: Springer Berlin Heidelberg; 1994, p. 165–92. http://dx.doi.org/10.1007/978-3-642-85167-4_10.

[53] Appel J, Bockhorn H, Frenklach M. Kinetic modeling of soot formation with detailed chemistry and physics: Laminar premixed flames of C2 hydrocarbons. Combust Flame. 2000;121(1–2):122–36. http://dx.doi.org/10.1016/S0010-2180(99)00135-2.

[54] Kazakov A, Frenklach M. Dynamic modeling of soot particle coagulation and aggregation: implementation with the method of moments and application to high-pressure laminar premixed flames. Combust Flame. 1998;114(3–4):484–501. http://dx.doi.org/10.1016/S0010-2180(97)00322-2.

[55] Yuan C, Laurent F, Fox R. An extended quadrature method of moments for population balance equations. J Aerosol Sci 2012;51:1–23. http://dx.doi.org/10.1016/j.jaerosci.2012.04.003.

[56] Wick A, Nguyen T-T, Laurent F, Fox RO, Pitsch H. Modeling soot oxidation with the extended quadrature method of moments. Proc Combust Inst 2017;36(1):789–97. http://dx.doi.org/10.1016/j.proci.2016.08.004.

[57] Ferraro F, Gierth S, Salenbauch S, Han W, Hasse C. Soot particle size distribution reconstruction in a turbulent sooting flame with the split-based extended quadrature method of moments. Phys Fluids 2022;34(7):075121. http://dx.doi.org/10.1063/5.0098382.

[58] Koob P, Nicolai H, Schmitz R, Hasse C. Analysis of potential soot breakthrough during oxidation at aero-engine relevant conditions. Proc Combust Inst 2024;40(1–4):105672. http://dx.doi.org/10.1016/j.proci.2024.105672.

[59] Marinov NM. A detailed chemical kinetic model for high temperature ethanol oxidation. Int J Chem Kinet 1999;31(3):183–220. http://dx.doi.org/10.1002/(SICI)1097-4601(1999)31:3<183::AID-KIN3>3.0.CO;2-X.

[60] Saxena P, Williams FA. Numerical and experimental studies of ethanol flames. Proc Combust Inst 2007;31(1):1149–56. http://dx.doi.org/10.1016/j.proci.2006.08.097.

[61] Schmitz R, Sirignano M, Hasse C, Ferraro F. Numerical investigation on the effect of the oxymethylene ether-3 (OME3) blending ratio in premixed sooting ethylene flames. Front Mech Eng 2021;7:744172. http://dx.doi.org/10.3389/fmech.2021.744172.

[62] Matti Maricq M. Soot formation in ethanol/gasoline fuel blend diffusion flames. Combust Flame. 2012;159(1):170–80. http://dx.doi.org/10.1016/j.combustflame.2011.07.010.